

# Exploring the High Entropy approach in $Mn_3Sn$

A Dissertation for

Course code and Course Title:PHY 651 Dissertation

Credits: 16

Submitted in partial fulfillment of Master's Degree

M.Sc in Solid State Physics

by

**FATIMA MYRIAM BARRETO**

Seat number: 22P0430010

ABC ID:234644844313

PRN:20190244

Under the supervision of

**DR.ELAINE T DIAS**

School Of Physical and Applied Science

Physics discipline



**Goa University**

May 2024



Examined by:

Seal of the School

## DECLARATION BY STUDENT

I hereby declare that the data presented in this Dissertation report entitled, "Exploring the High Entropy approach in  $Mn_3Sn$ " is based on the results of investigations carried out by me in the Physics Discipline at the School of Physical and Applied Sciences, Goa University under the Supervision of Dr. Elaine Dias and the same has not been submitted elsewhere for the award of a degree or diploma by me. Further, I understand that Goa University or its authorities will be not be responsible for the correctness of observations / experimental or other findings given the dissertation. I hereby authorize the University authorities to upload this dissertation on the dissertation repository or anywhere else as the UGC regulations demand and make it available to any one as needed.

*Barreto*

Signature and Name: Miss. Fatima Myriam Barreto

Seat No: 22P0430010

Date: 8/05/2024

Place: Goa University

## COMPLETION CERTIFICATE

This is to certify that the dissertation report "Exploring the High Entropy approach in  $Mn_3Sn$ " is a bonafide work carried out by Miss Fatima Myriam Barreto under my supervision in partial fulfillment of the requirements for the award of the degree of M.Sc in Physics at the School of Physical and Applied Sciences, Goa University.

Signature and Name of Supervisor: Dr Elaine T Dias

Date: 08.05.2024

Signature of Dean of the School:

Date: 8 | 05 | 24

Place: Goa University



School stamp:

## Acknowledgement

I express my deepest gratitude to my project guide, Dr. Elaine T Dias. I am very thankful to her for giving me this opportunity to work under her on this topic. Her constant support and guidance helped with the successful completion of the project.

I am extremely grateful to Dr. Kaustubh R. S. Priolkar, whose guidance during the dissertation provided invaluable insights, challenged my perspectives, and encouraged me to strive for excellence in my research endeavors.

A special thanks to all Ph.D. scholars for providing a happy and friendly environment and keeping me motivated all the time throughout the project especially, Myren Azavedo.

I also extend my sincere thanks to Miss. Elishka Vaz for her constant help throughout my project despite her busy schedule.

I also wish to thank all the teachers and non-teaching staff from the Physics Department for their help and support.

I am also thankful to my friends for their support. Lastly, I thank my parents for encouraging me to pursue my dreams.

## Abstract

In this project, we have explored the approach of introducing high entropy in  $Mn_3Sn$  alloys by replacing Mn with 5 elements such that the  $e/a$  ratio of these elements is equal to the number of valence electrons in Mn. The  $e/a$  ratio of V, Cr, Mn, Fe, and Co taken in equiatomic ratios was found to be equal to 7, which is equal to number of valence electrons in Mn. Thus an alloy with stoichiometric composition  $V_{0.2}Cr_{0.2}Mn_{0.2}Fe_{0.2}Co_{0.2}$  was chosen to prepare high entropy Mn. We started by establishing an underlying base for our project by preparing high entropy Fe ( $Cr_{0.2}Mn_{0.2}Fe_{0.2}Co_{0.2}Ni_{0.2}$ ) and establishing its results reported in the literature. Following this we prepared high entropy Mn and characterized it, which was the first main objective of the project. Later we aimed on synthesizing and characterizing high entropy  $Mn_3Sn$  and  $Fe_3Sn$  by replacing Mn and Fe with five elements respectively. For this two approaches were followed, One was preparing the alloy by melting all the elements together with Sn and annealing at  $1000^\circ C$  which was reported for the preparation of high entropy alloys. Second approach was by following the conventional  $Mn_3Sn$  and  $Fe_3Sn$  preparation by melting high entropy sample with Sn and annealing it at  $800^\circ C$ . X-ray diffraction characterization was carried out to understand the phases present in the resultant sample. Following this four probe resistivity measurements were done to understand the structural and magnetic transitions in the sample to understand its behavior with temperature.

# Contents

<b>List of Figures</b>	<b>iii</b>
<b>List of Tables</b>	<b>v</b>
<b>1 Introduction</b>	<b>1</b>
1.1 $\text{Mn}_3\text{X}$ . . . . .	1
1.2 $\text{Mn}_3\text{Sn}$ . . . . .	2
1.2.1 Properties of $\text{Mn}_3\text{Sn}$ . . . . .	3
1.3 High Entropy Alloys (HEAs) . . . . .	6
1.3.1 Phase structure of HEAs . . . . .	8
1.3.2 Studies on High Entropy alloys . . . . .	10
<b>2 Experimental Techniques</b>	<b>11</b>
2.1 Introduction . . . . .	11
2.2 Sample preparation . . . . .	12
2.2.1 Weights . . . . .	12
2.2.2 Sample cleaning . . . . .	13
2.2.3 Arc melting . . . . .	13
2.2.4 Weight loss and homogeneity check . . . . .	14
2.2.5 Vacuum sealing . . . . .	14
2.2.6 Annealing . . . . .	15
2.2.7 Quenching . . . . .	15
2.3 Characterization . . . . .	16
2.3.1 X-ray Diffraction . . . . .	16

<i>CONTENTS</i>	ii
2.3.2 Four probe method . . . . .	17
2.4 Data Analysis . . . . .	18
<b>3 Analysis</b>	<b>20</b>
3.1 High Entropy Fe . . . . .	20
3.2 High Entropy Mn . . . . .	23
3.3 High Entropy Mn-Sn alloy . . . . .	24
3.3.1 Annealed at 1000°C . . . . .	24
3.3.2 Annealed at 800°C . . . . .	26
3.4 High Entropy Fe-Sn alloy . . . . .	29
3.4.1 Annealed at 1000 ° C . . . . .	29
3.4.2 Annealed at 800°C . . . . .	31
<b>4 Conclusion</b>	<b>34</b>
<b>References</b>	<b>35</b>

# List of Figures

1.1	Mn <sub>3</sub> Sn structure [1]	2
1.2	Temperature dependence of magnetization in Mn <sub>3</sub> Sn	3
1.3	Resistivity dependence on temperature in Mn <sub>3</sub> Sn	4
1.4	Entropy increase in the development of materials	6
1.5	Phase structures of HEAs	8
1.6	Relationship between the VEC and the presence of $\sigma$ phase after aging for a number of HEAs	9
2.1	Arc Furnace	13
2.2	Bragg's law: Constructive interference	16
3.1	Sample pounded into a thin sheet	20
3.2	LeBail fit for high entropy Fe	21
3.3	Generated pattern of High entropy Fe	22
3.4	Reitveld refinement of High entropy Fe	23
3.5	Lebail fit for High entropy Mn	24
3.6	Sn melted out of the sample on annealing	24
3.7	Phases that matched with XRD data of Mn-Sn alloy	25
3.8	Mn-Sn phase diagram	26
3.9	Lebail fit for Mn-Sn alloy	27
3.10	Resistivity plot for Mn-Sn alloy	28
3.11	Sample fused together on annealing	29
3.12	Phases that matched with XRD data of Fe-Sn alloy	30
3.13	Fe-Sn phase diagram	31

3.14 LeBail Fit of the XRD data for Fe-Sn alloy . . . . .	32
3.15 Resistivity plot for High entropy Fe-Sn alloy . . . . .	33

# List of Tables

2.1	Weights of all the samples prepared . . . . .	12
2.2	Weight loss of the samples . . . . .	14
2.3	Annealing temperatures and days . . . . .	15
3.1	List of phases that matched the Mn-Sn XRD data . . . . .	25
3.2	List of phases that matched the Mn-Sn XRD data . . . . .	27
3.3	List of phases that matched the Fe-Sn XRD data . . . . .	30
3.4	List of phases that matched the Fe-Sn XRD data . . . . .	32

# Chapter 1

## Introduction

### 1.1 $\text{Mn}_3\text{X}$

$\text{Mn}_3\text{X}$  compounds where X= Ge, Sn, Ga, Ir, Rh, and Pt are compounds in which the magnetic Mn atoms forming AB-stacked kagome lattices have received a high attention since the observation of the anomalous hall effect has been reported in  $\text{Mn}_3\text{Ge}$  and  $\text{Mn}_3\text{Sn}$  [2]. The planes of Mn moments are arranged in a Kagome type lattice as a result of which these materials exhibit a noncollinear antiferromagnetic order, because of geometrical frustration, with respect to these Kagome planes, it was found that both the anomalous Hall conductivity (AHC) and the spin Hall conductivity (SHC) are anisotropic for any of these materials [3].

From a technological point of view these emergent transport properties of  $\text{Mn}_3\text{X}$  compounds are very attractive in the development of antiferromagnetic spintronics and memory devices [4]. Consequently, there have been several experimental and theoretical studies focused on determination of the magnetic ground state of  $\text{Mn}_3\text{X}$  compounds. Yasukochi and Ohoyama were the first to identify weak ferromagnetism in  $\text{Mn}_3\text{Sn}$  and  $\text{Mn}_3\text{Ge}$ . Later, the first neutron diffraction studies of these two compounds led to determination of the noncollinear  $120^\circ$  structure. Consecutive powder neutron diffraction experiments on  $\text{Mn}_3\text{Ga}$ ,  $\text{Mn}_3\text{Ge}$ , and  $\text{Mn}_3\text{Sn}$  also determined that the antiferromagnetic order and the induced magnetic moment are restricted to the

plane perpendicular to the  $c$  axis of the compound. Recent studies revealed that of the possible triangular magnetic structures, the ground state of these  $Mn_3X$  compounds is the antichiral “inverse triangular” structure. Novel techniques have been proposed for imaging and writing of magnetic domains in  $Mn_3Sn$  [5]. In this project will focus on  $Mn_3Sn$  and explore the high entropy approach in it.

## 1.2 $Mn_3Sn$

$Mn_3Sn$  a kagome antiferromagnet is an intermetallic compound which crystallizes in a hexagonal structure with space group  $P6_3/mmc$  as shown in Fig. 1.1. It is a topological Weyl semimetal which has been an active study topic since the discovery of the large anomalous Hall effect, large Nernst effect at room temperature, magnetic Weyl fermions, magnetic inverse spin Hall effects [1].

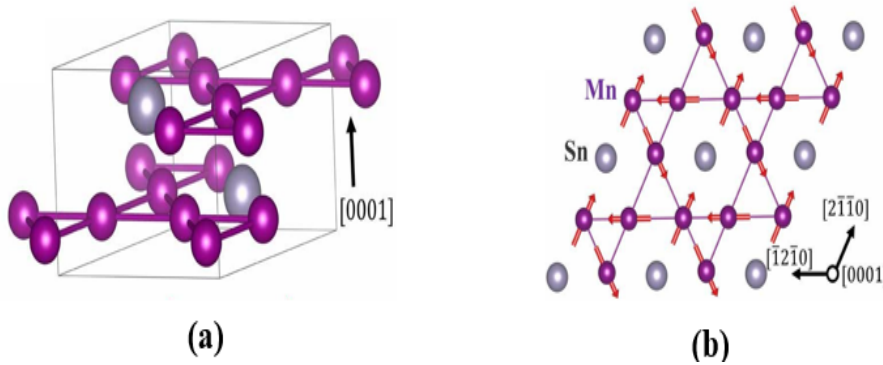


Figure 1.1:  $Mn_3Sn$  structure [1]

### Kagome Lattice

$Mn_3Sn$  crystallizes in a hexagonal lattice with a kagome antiferromagnetic structure. This lattice consists of corner-sharing triangles and is characterized by a large degree of geometric frustration, while two of the three spins can be antiparallel, the third one is frustrated and aligns at  $120^\circ$  with respect to the other spin resulting in weak ferromagnetism as shown in Fig. 1.1(b). In every unit cell of  $Mn_3Sn$ , manganese atoms form a frustrated kagomé lattice with tin atoms occupying the center positions and Mn occupying the corners of the lattice [6]. This lattice structure leads to frustration because there’s no way for all the spins to align in a single,

low-energy configuration due to competing interactions between neighboring spins. These materials have gained significant interest for potential applications in quantum computing and spintronics due to their unique magnetic properties.

### 1.2.1 Properties of $Mn_3Sn$

$Mn_3Sn$  has two interesting properties, that is temperature dependence of magnetization and resistivity.

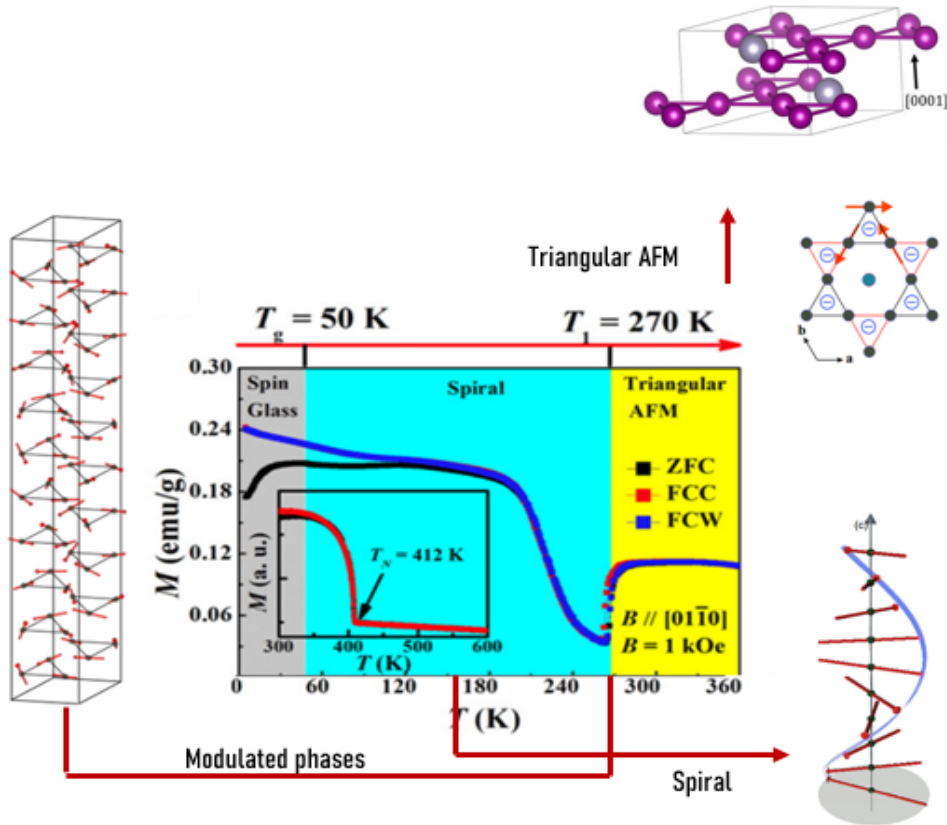


Figure 1.2: Temperature dependence of magnetization in  $Mn_3Sn$

#### Temperature dependence of magnetization

$Mn_3Sn$  is an antiferromagnet having Neel temperature above 400K. It was seen that as the sample is cooled the compound undergoes a magnetic transition at  $T_1 = 290K$  as shown in Fig. 1.2. This transition corresponds to the magnetostructural phase transition from the triangular antiferromagnet structure to the modulated phases. Initially, no difference between ZFC and FCW was observed implying that the struc-

ture  $T_1$  is still antiferromagnetic. Below 215K the magnetization was observed to increase again due to anisotropy change of double helix magnetic structure. With further decrease in temperature, a slight drop in magnetization is observed around 40K in the ZFC curve, this indicates the glassy ferromagnetic like state reported for the alloy [7].

### Temperature dependence of resistivity

The resistivity of  $Mn_3Sn$  shows metallic like behavior with electric current applied. As the temperature was increased a kink was observed at magnetic transition temperature  $T_1$ . The inset shows the hysteresis of  $\rho$  near  $T_1$  upon warming and cooling, which indicates a first-order phase transition[7].

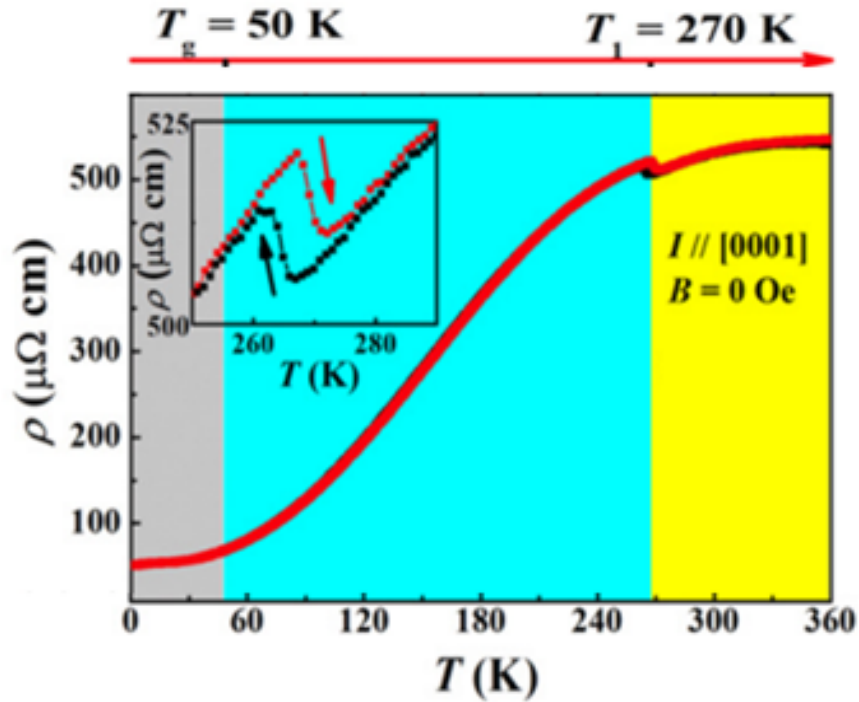


Figure 1.3: Resistivity dependence on temperature in  $Mn_3Sn$

### Effect of doping $Mn_3Sn$

Interesting properties were reported on doping  $Mn_3Sn$  with transition metals Fe, Cr at Mn site. It was observed that topological properties of strongly correlated antiferromagnet  $Mn_3Sn$  could be tuned via Fe doping. In [8] the electronic, magnetic, and topological properties of  $Mn_{3-x}Fe_xSn$  were reported by varying the concentration of x. It was observed that on increasing the concentration of Fe ferromagnetism was introduced in the system. Resistivity studies showed a metal to insulator-like transition and resistivity upturns with increase in x at the reported transition temperatures. Large uniaxial magnetocrystalline anisotropy was induced by the Fe doping along with competing magnetic interactions at low temperature. This gave nontrivial spin texture, leading to a large topological Hall effect in the doped systems at low temperatures.

Coexistence of in-plane and out-of-plane exchange bias in correlated kagome antiferromagnet  $Mn_{3-x}Cr_xSn$  studied in [9]. On increasing the percentage of Cr in  $Mn_3Sn$  and in turn increasing the electron per atom ratio(e/a) coexistence of antiferromagnet and ferromagnetic phase was observed at low temperature region. Field-cooling experiments conducted by applying field parallel and perpendicular to the frustrated Kagome plane displayed loop shifts and enhanced coercivities. The results reported suggested that the exchange bias along perpendicular kagome plane is primarily induced by Dzyaloshinskii-Moriya interactions due to the breaking of interfacial symmetry, while the exchange bias effect along kagome plane is due to the exchange effects at interface of antiferromagnet and ferromagnet component originating from the net moment.

On comparing these results to the undoped  $Mn_3Sn$  structure we can see how the triangular antiferromagnet on doping shows enhanced characteristics of ferromagnetism for different concentrations of Cr and Fe as the e/a ratio changes significantly. In case of Fe doped  $Mn_3Sn$  the resistivity behaviour showed a change from metal like behaviour for  $Mn_3Sn$  to a metal to insulator like transition for  $Mn_{3-x}Fe_xSn$ .

### 1.3 High Entropy Alloys (HEAs)

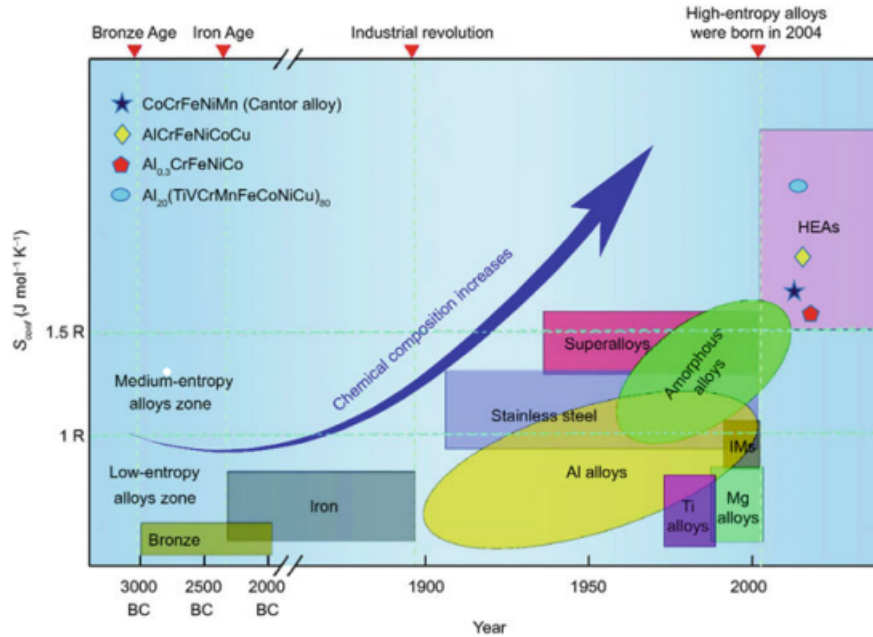


Figure 1.4: Entropy increase in the development of materials

An alloy is formed when a metal is combined with other substances to create a new metal with enhanced properties. Conventional alloys contain one or two main elements which may be stronger, harder, tougher, or more malleable than the original metal. For example, steel is formed by combining iron with another element such as carbon. This combination showed enhanced strength, hardness, and other desirable properties compared to pure iron. On observing how the addition of small amount of an element to the material showed a great change in properties, the concept of high entropy alloys (HEAs) came through [10].

HEAs contain five or more elements in equiatomic/ non equiatomic ratios, resulting in a complex microstructure and high configurational entropy. Development of these materials showed interesting properties like high ductility, high strength and corrosion resistance. As we know entropy is a measure of randomness or disorder of a system, in these alloys we try to increase the disorder by increasing the number of elements. High configurational entropy arises from the number of ways the atoms can be arranged in a system.

To prepare high entropy alloys the following criteria have to be followed [10]:

**1. Compositional requirements:**

The alloy should have at least five major metal elements, each having an atomic percentage of 5–35 %.

$$n_{major} \geq 5, 5at.\% \leq c_i \leq 35at.\%$$

$$n_{minor} \geq 0, c_j \leq 5at.\%$$

$n_{major}$  - number of primary elements ,  $n_{minor}$  - number secondary elements  
and  $c_i, c_j$  - atomic percentages of major and minor elements respectively.

Addition of minor element is optional according to desired property enhancement.

**2. Concept of entropy:**

The entropy of a system in a given state can be written as

$$S = k \ln W$$

$$k = R/N_A$$

$k$ = Boltzman constant,  $S$ = Configurational entropy,  $W$ =number of real microsates corresponding to macrostates and  $R$ = molar gas constant.

HEAs need to have configurational entropy larger than  $1.61R$  in their random solution state.

$$\Delta S_{mix} \geq 1.6R$$

### 1.3.1 Phase structure of HEAs

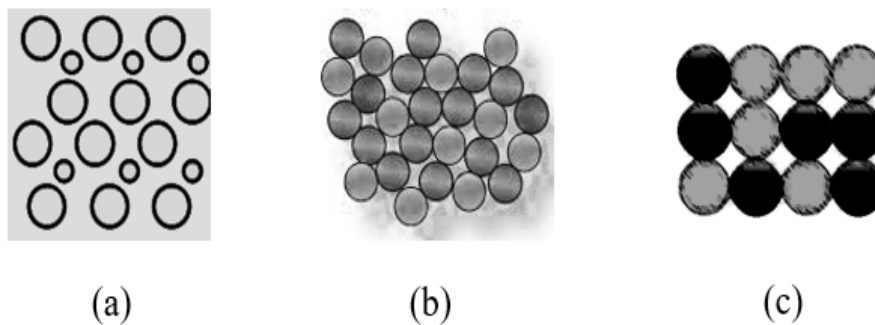


Figure 1.5: Phase structures of HEAs

High entropy alloys can form different categories of phase structures. It can form intermetallic compounds as shown in Fig.1.5.a which have two or more metallic elements combined in a specific stoichiometric ratio. Secondly it can form a disordered atomic or molecular structure namely, amorphous alloy as shown in Fig. 1.5.b. However, with the deepening of research on HEAs, it has been found that many HEAs systems do not produce numerous intermetallic compounds and other complex structural phases during solidification[10]. In contrast, HEAs tend to produce alloy solid solution phases as shown in Fig. 1.5.c with a simple structure.

#### Solid Solution HEAs

Solid solution phase is a homogeneous mixture of two different kinds of atoms in solid state forming a single crystal structure. These alloys further crystallize into body centered cubic(BCC), Face centered cubic (FCC), Hexagonal closed packed structure (HCP), Sigma phase( $\sigma$ ) or a combination of these phases. For instance, elements used for alloying in HEAs; Cu, Al, Ni are FCC-type, Fe, Cr, Mo, V are BCC-type and Ti, Co are HCP type at ambient temperature. When these elements are mixed with different combination in different amounts of certain elements fcc, bcc or mixed fcc and bcc structures may form.[11] CoCrCuFeNi a high entropy Fe alloy formed a FCC structure.[12] AlCoCrCuFeNi showed characteristics of both FCC and BCC structure. It was reported that on increasing Al concentration the crystal structure tuned from fcc to fcc plus bcc to fully bcc.

**Sigma Phase:**

Recent studies have shown that the as-cast solution phases in HEAs may transform to intermetallic phases [13] when aged at intermediate temperatures. The formation of sigma phase is frequently observed in aged HEAs. It is a tetragonal intermetallic phase containing 30 atoms per unit cell [11]. It leads to material hardening, which could be favorable under certain circumstances. The compositional range of its stability is governed by  $e/a$  ratio and valence electron concentration (VEC). In the case of 3d HEAs, the Cantor alloy itself is found to be highly stable in the fcc structure and undergoes a transition to the  $\sigma$  phase when annealed around 700 degree celcius for longer time periods.

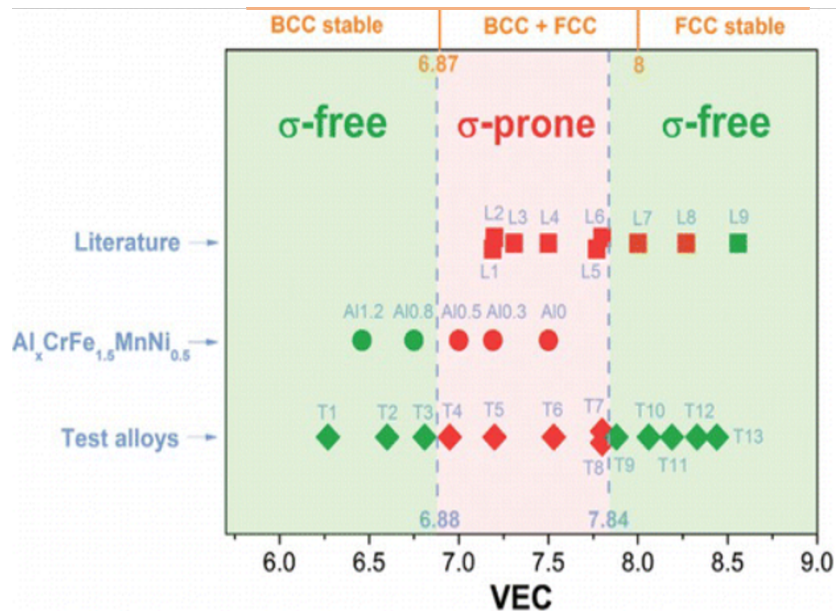


Figure 1.6: Relationship between the VEC and the presence of  $\sigma$  phase after aging for a number of HEAs

Green and red icons in Fig. 1.6 indicate the absence and presence of  $\sigma$  phase after aging, respectively. The aging condition for the  $\text{Al}_x\text{CrFe}_{1.5}\text{MnNi}_{0.5}$  alloys and the test alloys is  $700^\circ\text{C}$  for 20hrs. From here we can conclude that VEC between 6.87 to 8 is more prone to  $\sigma$  phase formation. This falls into the range where Fe-Cr, Fe-V, and Mn-V alloys also exhibit the  $\sigma$  phase. It is also the range within which Mn and binary 3d-Mn alloys form complex cubic A12 ( $\alpha$ -Mn) and A13 ( $\beta$ -Mn) phases with 58 and 20 atoms per unit cell, respectively.

### 1.3.2 Studies on High Entropy alloys

The magnetic and structural properties of equiatomic and off-equiatomic high-entropy alloys  $\text{Cr}_{20+x}\text{Mn}_{20}\text{Fe}_{20}\text{Co}_{20}\text{Ni}_{20-x}$  were studied [11]. The composition dependent transformation from the FCC to  $\sigma$  phase with increasing  $x$  for off-equiatomic composition was reported. The FCC-Cantor alloy had the same valence-electron concentration ( $e/a$ : electrons per atom) as FCC-Fe with  $(e/a)=8$  and exhibits temperature-dependent properties that are actually predicted for FCC-Fe. Low-field (5 mT) temperature-dependent magnetization measurements  $M(T)$  revealed features related to the intrinsic magnetic interaction.

A High-Entropy B2 Heusler Alloy  $(\text{MnFeCoNiCu})_{75}\text{Al}_{25}$  was studied [14]. The properties of the resultant high entropy alloy showed systematic evolution with varying valence electron configurations. It formed mixed FCC–BCC phases with the BCC phase exhibiting B2 ordering in some cases. It was seen that this high entropy combination forms a stabilized pseudo- $\text{Co}_3\text{Al}$  compound with  $e/a = 7.5$  which is reported to be unstable otherwise.

Magnetic, structural, hardness and thermal expansion properties of the FCC and BCC phases of  $(\text{MnFeCoNi})_{80}\text{Cu}_{20-x}\text{Z}_x$  ( $Z=\text{Al}, \text{Ga}$ ) high-entropy alloys were studied [15]. In this case, base alloy  $(\text{MnFeCoNi})_{80}\text{Cu}_{20}$  composed of all-3d-transition metals was taken, and the effect of Al and Ga-substitution as main group elements in place of Cu was seen. On increasing Al and Ga content in the base alloy, the structure was seen to be more ordered taking up body-centered positions of the BCC lattice. Additionally, these structures were known to exhibit similar physical properties like Invar property with low thermal expansion coefficient with the 3d-transition metal-alloys having the same valence electron concentration.

From the above literature review we can observe that high entropy alloys formed on combining with another element enhanced the properties of the resultant sample leading to its application in many advanced fields of science.

# Chapter 2

## Experimental Techniques

### 2.1 Introduction

The current chapter categorically details the procedure involved in the synthesis of high entropy alloys along with the different experimental techniques used for the characterization of the prepared alloys. To begin with, the diffraction experiments using x-ray radiations as a source are described, which were performed for structure analysis. Four probe resistivity method was used to study the transport properties.

The list of compositions prepared in equiatomic ratios and later combined with Sn is as follows:

1. High Entropy alloys

S1	High Entropy Fe	$\text{Cr}_{0.2}\text{Mn}_{0.2}\text{Fe}_{0.2}\text{Co}_{0.2}\text{Ni}_{0.2}$
S2	High Entropy Mn	$\text{V}_{0.2}\text{Cr}_{0.2}\text{Mn}_{0.2}\text{Fe}_{0.2}\text{Co}_{0.2}$

2. High Entropy alloys combined with Sn

S3	$\text{Mn}_3\text{Sn}$	$(\text{V}_{0.2}\text{Cr}_{0.2}\text{Mn}_{0.2}\text{Fe}_{0.2}\text{Co}_{0.2})_3\text{Sn}$
S4	$\text{Mn}_3\text{Sn}$	$(\text{High Entropy Mn})_3\text{Sn}$
S5	$\text{Fe}_3\text{Sn}$	$(\text{Cr}_{0.2}\text{Mn}_{0.2}\text{Fe}_{0.2}\text{Co}_{0.2}\text{Ni}_{0.2})_3\text{Sn}$
S6	$\text{Fe}_3\text{Sn}$	$(\text{High Entropy Fe})_3\text{Sn}$

## 2.2 Sample preparation

### 2.2.1 Weights

The elements were weighed according to the stoichiometric proportions as shown in the table below:

Sample	Elements	Calculated (g)	Normalized (g)	Sample weight
S1	Cr	0.1236	0.1811	0.9633
	Mn	0.1306	0.1914	
	Fe	0.1328	0.1946	
	Co	0.1401	0.2053	
	Ni	0.1396	0.2063	
	Total weight	1.0000	0.9787	
S2	V	0.1868	0.1893	1.0001
	Cr	0.1907	0.1932	
	Mn	0.2015	0.2042	
	Fe	0.2048	0.2075	
	Co	0.2161	0.2190	
	Total weight	1.0000	1.0132	
S3	V	0.1083	0.1093	1.0004
	Cr	0.1105	0.1155	
	Mb	0.1168	0.1179	
	Fe	0.1187	0.1198	
	Co	0.1253	0.1265	
	Sn	0.4205	0.4245	
	Total weight	1.0000	1.0097	
S4	High entropy Mn	0.8720		1.4977
	Sn	0.6281		
	Total weight	1.5002		
S5	Cr	0.1087	0.1093	1.0038
	Mn	0.1149	0.1155	
	Fe	0.1168	0.1175	
	Co	0.1232	0.1239	
	Ni	0.1228	0.1235	
	Sn	0.4136	0.4160	
	Total weight	1.0000	1.0057	
S6	High entropy Fe	0.8780	0.5475	0.9253
	Sn	0.6221	0.3879	
	Total weight	1.5001	0.9354	

Table 2.1: Weights of all the samples prepared

### 2.2.2 Sample cleaning

Iron(Fe), Chromium(Cr), Manganese(Mn) and Vanadium(V) from Alfa Aesar company having 99.9% purity were cleaned before sample preparation to remove any oxide layer present on the surface. Fe, Mn, Cr placed in beakers containing a metal cleaning solution. The beakers were then placed in an ultrasonicator for 15 minutes to facilitate the removal of surface oxidation. Following this, the metal pieces were washed in isopropyl alcohol. This process is repeated until the metal appears shiny and clean. A similar procedure was followed for cleaning vanadium but the excess oxide was first scrapped off using a blade before placing in the metal cleaning solution.

### 2.2.3 Arc melting



Figure 2.1: Arc Furnace

In this process required elements were placed in the copper hearth according to their vapour pressure and oxidation state [16]. Following this, vacuum cycle was run for 15 minutes and the Argon cycle was run for 10 minutes. These cycles were repeated 3 times to maintain a controlled inert gas atmosphere. Next, an electric current was passed between two electrodes which generated intense heat, causing the elements placed in the copper hearth to reach its melting point, resulting in its transformation from a solid state to a liquid state. Throughout this process, the chiller is kept on to maintain the cooling of the copper hearth balancing out the excess heat generated. Once the melting has been achieved, the power to the arc is turned off, allowing the molten material to cool and solidify. The sample is flipped and this process is

repeated three times to maintain homogeneity of the sample prepared. After all the melting cycles are done the sample is kept for 30 minutes undisturbed to ensure internal homogeneous cooling before removing the sample out.

#### 2.2.4 Weight loss and homogeneity check

Weight loss for each sample was calculated and reported as follows 2.1:

Sample	Weight loss(%)
S1	1.57
S2	1.29
S3	0.92
S4	0.17
S5	0.19
S6	1.08

Table 2.2: Weight loss of the samples

Samples with weight loss less than three percent are considered. The samples were further cut into halves using a diamond cutter and checked for any phase separation present on the surface.

#### 2.2.5 Vacuum sealing

The sample was put in quartz tubes and sealed. To seal these tubes we need to create high vacuum so we, First open one valve of the rotary pump to evacuate the chamber. After closing this pump we open the next valve so that air from the upper tube system where the sample tubes are loaded is evacuated. Next, we open both the valves so that the whole system is fully evacuated. During final sealing, we need a high vacuum, so the diffusion pump is turned on. The oil in the lower chamber of the diffusion pump gets heated, the vapors rise up and after it reaches a certain level it cools and settles down back and this continuous process creates a high vacuum desired to seal the tubes [17].

### 2.2.6 Annealing

The sealed sample tubes are put in the furnace for a number of days at a certain temperature depending on the composition of the sample. The ramping rate is set to  $10^\circ / \text{min}$ . This annealing is done to ensure the removal of any strain present in the sample.

Sampl	Temperature	days
S1	1000 °C	3
S2	1000 °C	3
S3	1000 °C	2
S4	800 °C	3
S5	1000 °C	2
S6	800 °C	3

Table 2.3: Annealing temperatures and days

### 2.2.7 Quenching

Quenching is a process in which the sample is removed from the furnace and directly placed in water at room temperature or ice water to achieve rapid cooling. This is done to maintain mechanical properties linked with a crystalline structure or phase distribution that would be lost upon slow cooling. Samples S1, S2, S3, S5 were quenched in water at room temperature and samples S4 and S6 were quenched in ice water.

After annealing the sample is taken out and used as per requirements for further characterization.

## 2.3 Characterization

### 2.3.1 X-ray Diffraction

X-ray diffraction (XRD) is a non-destructive technique used to analyze material properties like phase composition, preferred crystal orientations, and other structural parameters [18]. In our experiment we have used Rigaku diffractometer to record data at room temperature using Cu K  $\alpha$  radiation (wavelength = 1.54 Å). The peaks are produced by constructive interference of a monochromatic beam of X-rays scattered at specific angles from each set of lattice planes in a sample. The intensities of each peak are determined by the distribution of atoms within the lattice. The data recorded was further analysed by doing Rietveld refinement to identify the phases present by comparing the diffraction pattern obtained with a reference from literature.

#### Bragg's law and diffraction

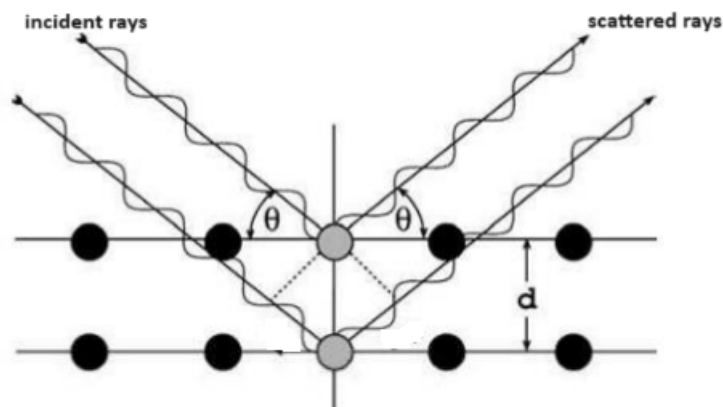


Figure 2.2: Bragg's law: Constructive interference

Bragg's Law gives a relationship between the angles of incidence and the wavelengths of X-rays or neutrons that are diffracted by a crystal lattice.

$$n\lambda = 2d\sin\theta \quad (2.1)$$

$n$  : integer representing the order of the diffraction peak.

$\lambda$  : wavelength of the incident radiation

$d$  : is the spacing between atomic planes within the crystal lattice.

$\theta$ : angle of incidence between the incident radiation and the crystal lattice planes.

The above equation states that constructive interference occurs when the path difference between the waves diffracted from adjacent atomic planes is an integer multiple of the wavelength. As a result, diffracted waves reinforce each other, leading to intensity peaks in the diffracted pattern.

### 2.3.2 Four probe method

A four point probe is typically used to measure the sheet resistance of a thin layer or substrate in units of ohms per square by forcing current through two outer probes and reading the voltage across the two inner probes [19] .

**Principle:** Depending upon the resistance of each sample, a current ( $I$ ) from the constant current source is passed through the two current probes and the potential drop  $V$  across the two voltage probes is measured. As negligible current is drawn by the voltmeter, the resistance  $R$  across the sample is measured using Ohm's law, ( $V = IR$ ) .Further, the electrical resistivity is measured using the relation,

$$\rho = RA/l$$

where  $l$  is the length and  $A$  is the area of cross section of the sample.

The resistivity measurements were carried out on thin rectangular cut alloy pieces, in the temperature range of 30 - 450 K by passing a current of 100mA, using conventional D.C four probe setup in a closed cycle refrigerator.

## 2.4 Data Analysis

The crystal structure solution was obtained through LeBail and Reitveld methods using FullProf Suite 2024. A hypothetical model was generated based on the crystallographic space group consisting of lattice constants, atomic site occupancies, fractional coordinates, etc of the data available. These parameters were further iteratively refined by the Least Square method based on the minimisation of the residual  $S$  between experimental and calculated patterns.

$$S_y = \sum_i w_i (y_i - y_{ci})^2$$

where,  $w_i = 1/y_i$ ,  $y_i$  = observed intensity and  $y_{ci}$  = calculated intensity

$$y_{ci} = s \sum_k L_k |F_k|^2 \phi(2\theta_i - 2\theta_k) P_k A + y_{bi}$$

where,  $s$ =scale factor,  $k$ =Miller indices( $h k l$ ),  $\phi$ =Reflection profile Function  $A$ =absorption factor,  $L_k$ = Lorentz polarization and multiplicity factors  $P_k$ =preferred orientation function,  $F_k$ =Structure factor for the  $K$ th Bragg reflection,  $y_{bi}$ =Background intensity at the  $i$ th step.

$$F_{hkl} = \sum_j N_j f_j e^{2\pi i(hx_j + ky_j + lz_j)} e^{-B \frac{\sin^2 \theta}{\lambda^2}}$$

where,  $N_j$  represents the site occupancy,  $B$  the temperature factor,  $f_j$  the structural factor and  $x_j, y_j, z_j$  the coordinates of the  $j$ th atom.

A good fit of the data is characterised by following reliability factors :

$$R_p = \frac{\sum |y_{io} - y_{ic}|}{\sum y_{io}}$$

$$R_{wp} = \left[ \frac{\sum w_i (y_{io} - y_{ic})^2}{\sum w_i y_{io}^2} \right]^{\frac{1}{2}}$$

$$R_{Bragg} = \frac{\sum |I_{ko} - I_{kc}|}{\sum I_{ko}}$$

$$R_{exp} = \left[ \frac{(N - P)}{\sum w_i y_{io}^2} \right]^{\frac{1}{2}}$$

$$\chi^2 = \frac{\sum w_i (y_{io} - y_{ic})^2}{N - P}$$

$R_p$  of the diffraction pattern (minimised during fitting procedures),  $R_{wp}$  (weighted to emphasise intense peaks over background),  $R_{Bragg}$  (tries to modify the R for a specific phase),  $R_{exp}$  (estimates the best value R for a data set) and reduced  $\chi^2$  (Goodness of fit).

# Chapter 3

## Analysis

### 3.1 High Entropy Fe



Figure 3.1: Sample pounded into a thin sheet

High Entropy Fe prepared with equiatomic ratio of  $\text{Cr}_{0.2}\text{Mn}_{0.2}\text{Fe}_{0.2}\text{Co}_{0.2}\text{Ni}_{0.2}$  was malleable. XRD characterization was carried out on a thin slice that was cut and pounded into a thin sheet.

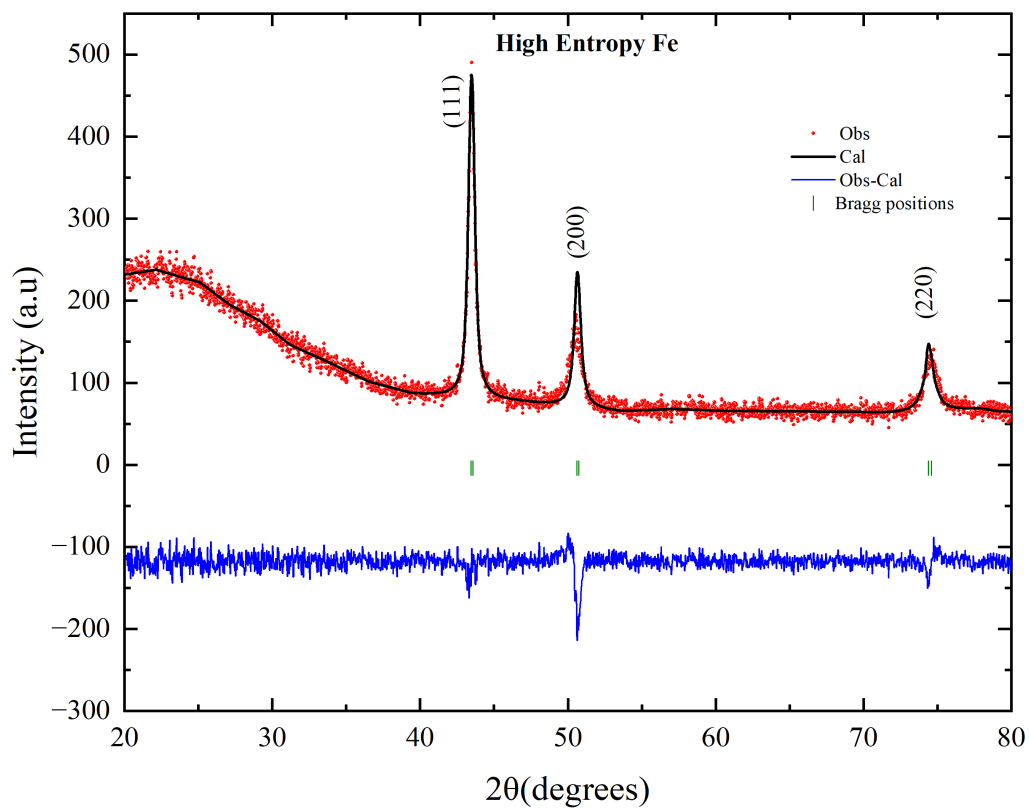


Figure 3.2: LeBail fit for high entropy Fe

Profile fitting of room temperature XRD pattern of high entropy Fe is shown in Fig. 3.2. The sample crystallizes into reported FCC Fe structure with space group  $Fm-3m$  and lattice constants  $a=b=c=3.6045 \pm 0.0002 \text{ \AA}$ .

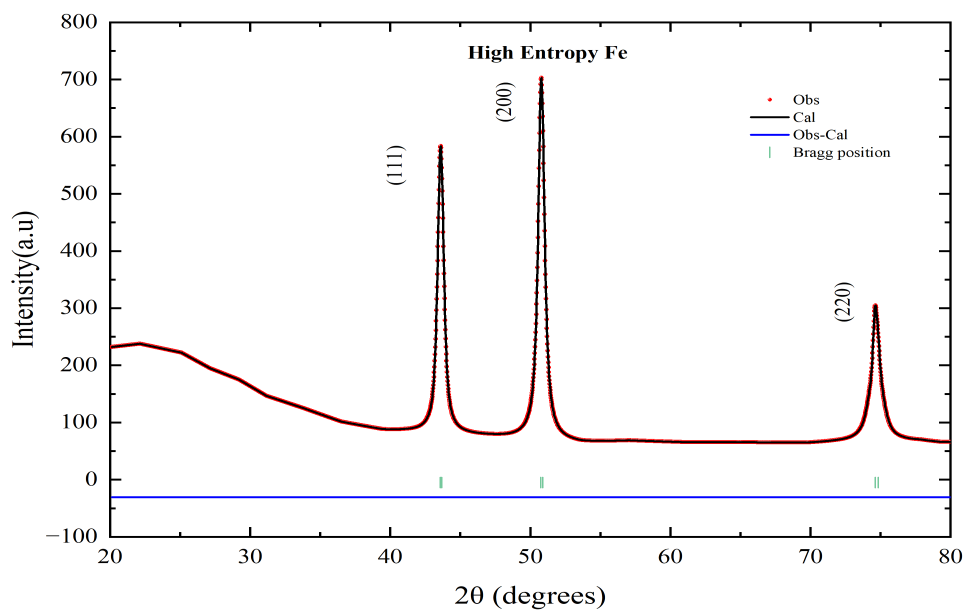


Figure 3.3: Generated pattern of High entropy Fe

To analyse the data further, a pattern was generated using general atomic positions ( $X=0, Y=0, Z=0$ ) and occupancy=1 of Fe. Reitveld refinement of high entropy Fe is shown in Fig. 3.4. On comparing the generated and Rietveld refinement graphs it was observed that the calculated and observed peak intensities do not match as in the generated pattern. This can be justified because of the preferred orientation as a thin pounded sheet of the sample was used for XRD characterization.

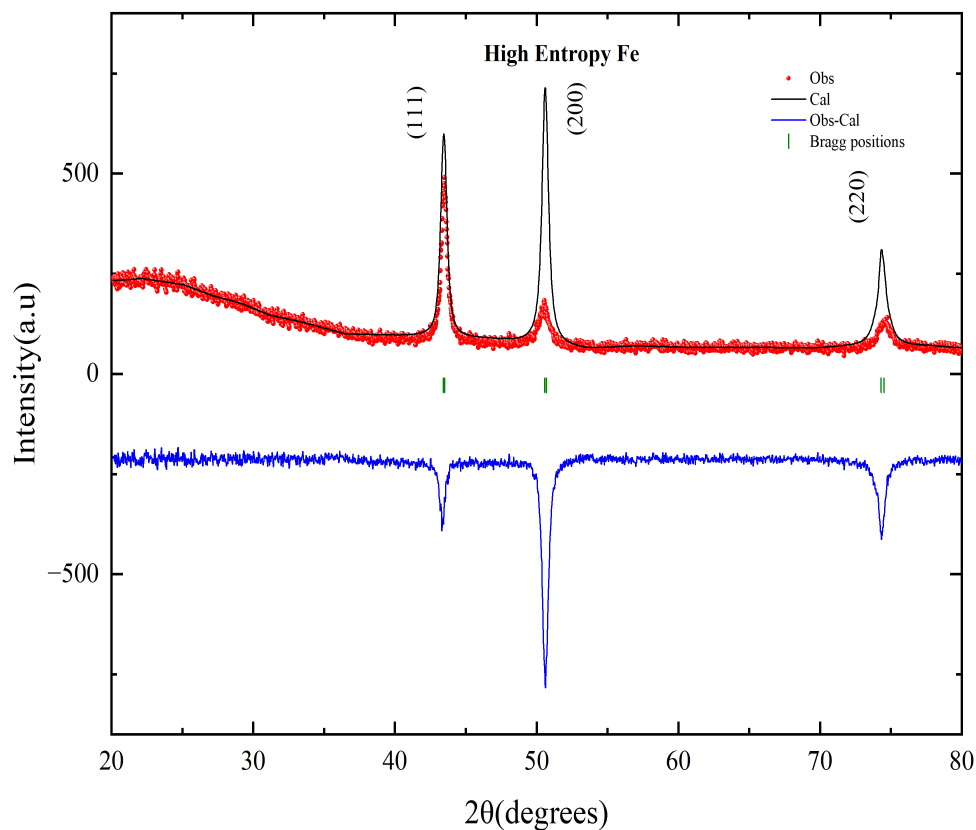


Figure 3.4: Reitveld refinement of High entropy Fe

## 3.2 High Entropy Mn

Profile fitting of room temperature XRD pattern of high entropy Mn is shown in Fig. 3.5. The sample crystallizes into a tetragonal structure with space group:  $P4_2/mnm$  and lattice constants  $a=b=8.8481 \pm 0.0001 \text{ \AA}$ ,  $c=4.5744 \pm 0.0001 \text{ \AA}$ . From [20] this phase can be classified as sigma phase with complex tetragonal structure having 30 atoms per unit cell.

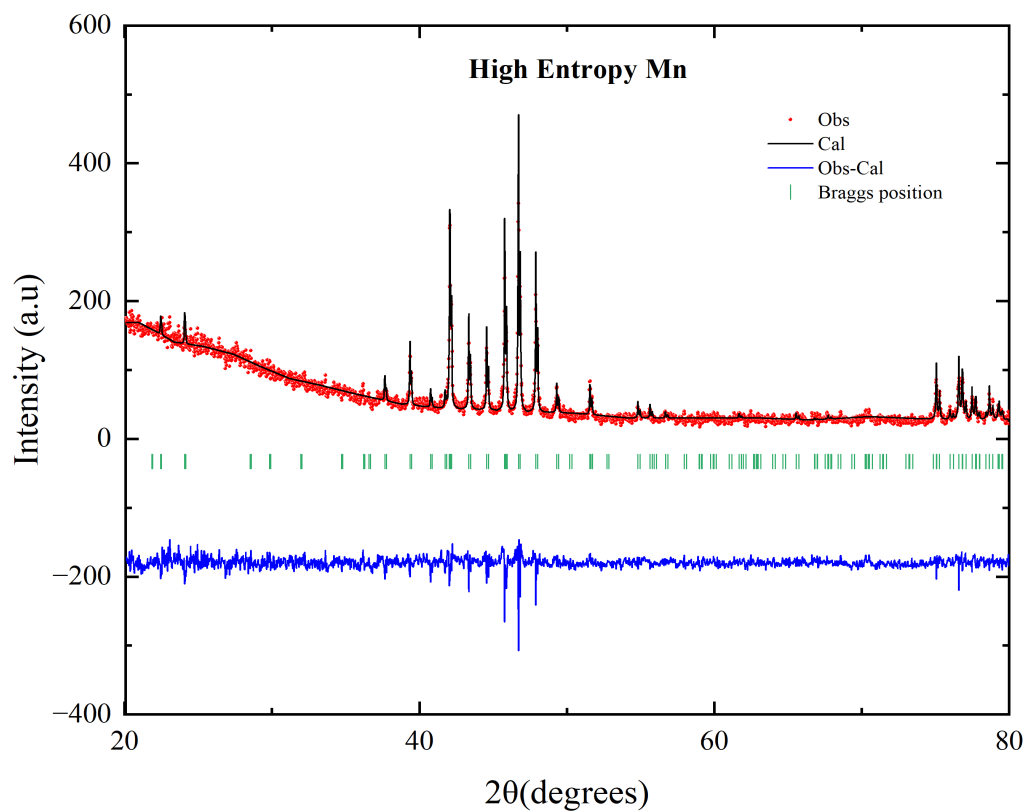


Figure 3.5: Leball fit for High entropy Mn

### 3.3 High Entropy Mn-Sn alloy

#### 3.3.1 Annealed at 1000°C



Figure 3.6: Sn melted out of the sample on annealing

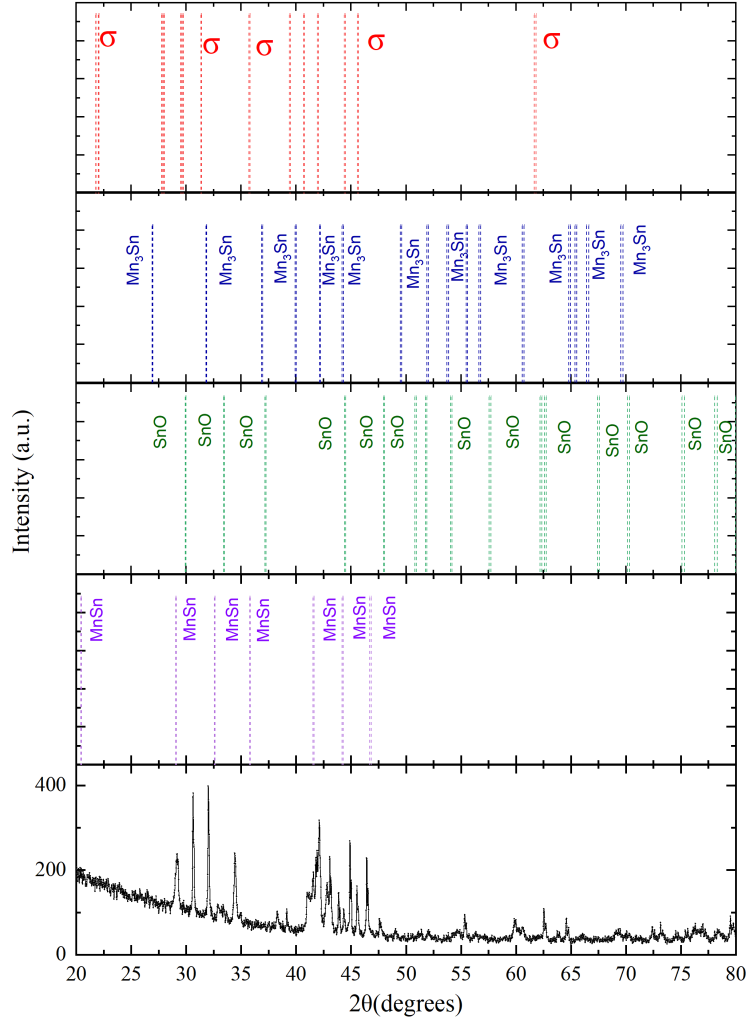


Figure 3.7: Phases that matched with XRD data of Mn-Sn alloy

Phases	Space group	Lattice constants( $\text{\AA}^\circ$ )
$\sigma$ phase	$P4_2/mnm$	$a=b=9.023 \pm 0.005, c=4.572 \pm 0.003$
$Mn_3Sn$	$P6_3/mmc$	$a=b=5.6264 \pm 0.0002, c=4.5128 \pm 0.0004$
SnO	$P4/nmm$	$a=b=3.7921 \pm 0.0006, c=4.8371 \pm 0.0002$
MnSn	$F-43m$	$a=b=c=6.1442 \pm 0.0003$

Table 3.1: List of phases that matched the Mn-Sn XRD data

On melting individual elements along with Sn and annealing, it was observed that the sample melted in the tube as shown in Fig. 3.6. Profile fitting of this data showed multiple phases as listed in 3.1. Most of the high intensity peaks matched with  $\sigma$  phase and SnO indicating that Sn leached out of the sample at high temperature and the other four elements combined giving a sigma phase character as reported for high entropy Mn.

## 3.3.2 Annealed at 800°C

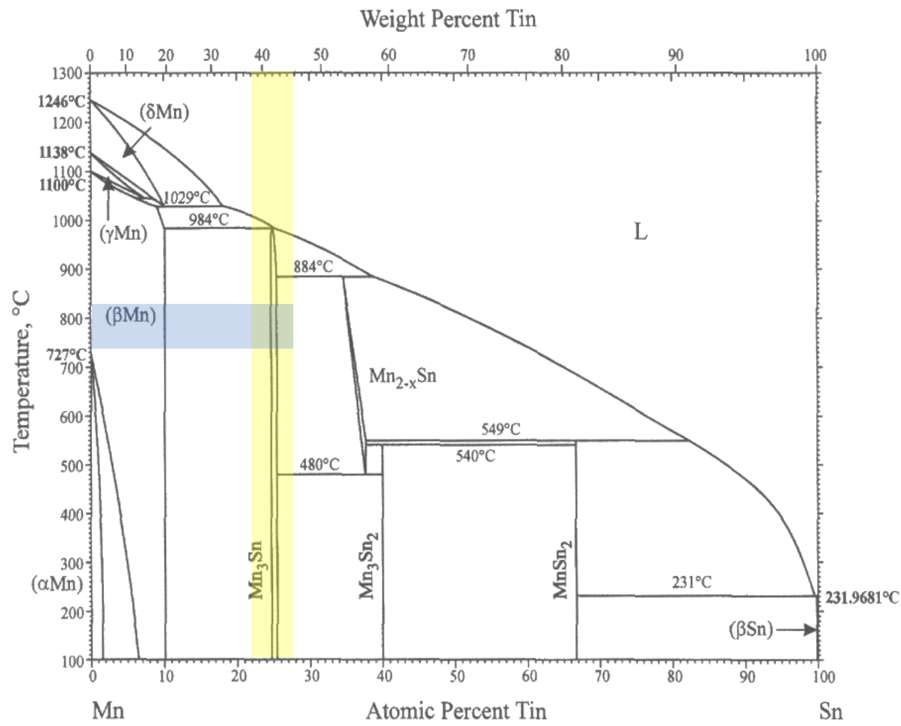


Figure 3.8: Mn-Sn phase diagram

The above Mn-Sn phase diagram [21] gives an information about the different phases formed at different annealing temperatures and concentration of Sn. The conventional weight percentage of Sn and annealing temperatures for synthesizing Mn<sub>3</sub>Sn were considered to prepare high entropy Mn<sub>3</sub>Sn and the results were recorded.

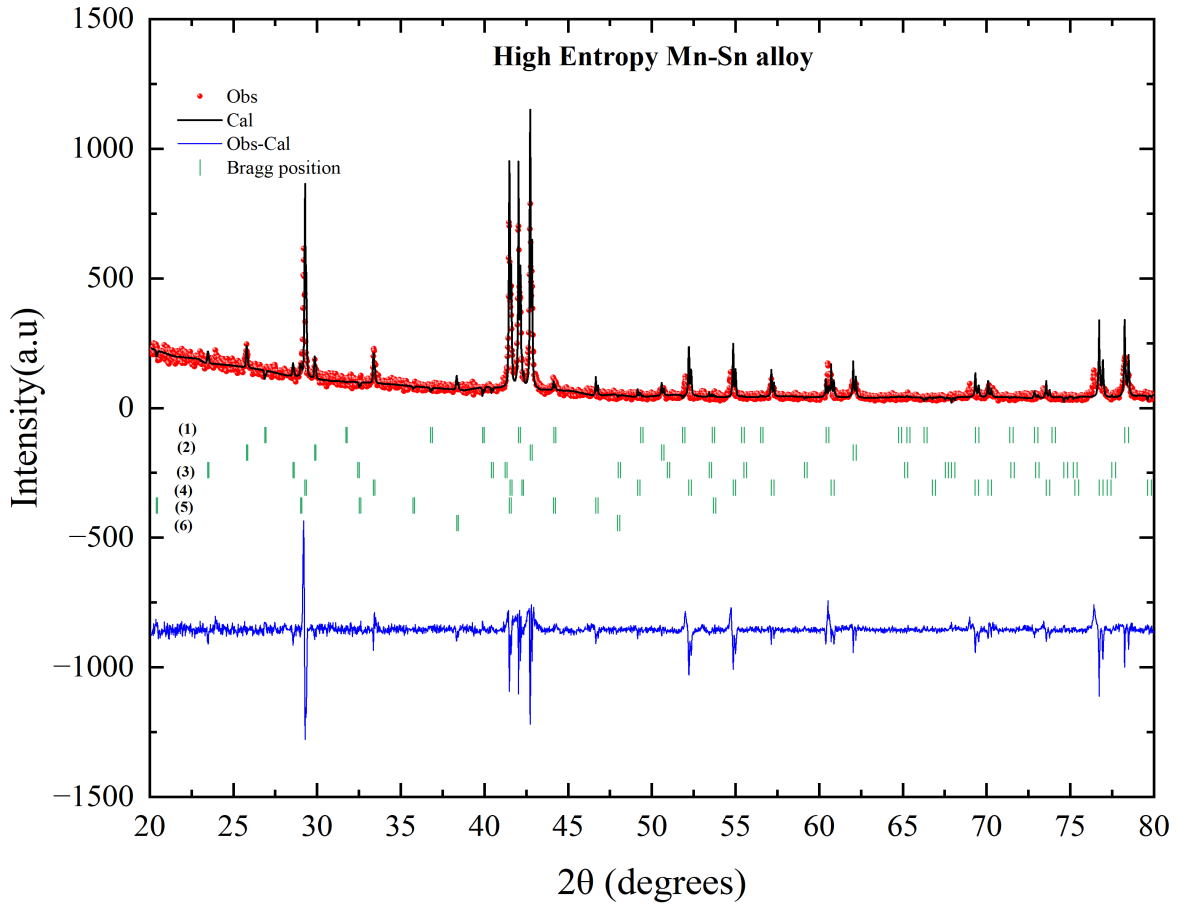


Figure 3.9: Leball fit for Mn-Sn alloy

Profile fitting of room temperature XRD pattern of high entropy Mn-Sn alloy is shown in Fig. 3.9 suggested presence of multiple phases as listed below. This indicated instability of the compound to form pure high entropy  $\text{Mn}_3\text{Sn}$  leading to an Mn-Sn alloy showing multiple phases.

No	Phases	Space group	Lattice constants( $\text{\AA}^\circ$ )
1)	$\text{Mn}_3\text{Sn}$	$P6_3/mmc$	$a=b=5.6380 \pm 0.0001, c=4.5182 \pm 0.0006$
2)	$\text{Mn}_2\text{Ni}_{2.35}\text{Sn}_{0.65}$	$Fm-3m$	$a=b=c=5.9796 \pm 0.0001$
3)	$\text{Mn}_2\text{Sn}$	$P6_3/mmc$	$a=b=4.374 \pm 0.001, c=5.516 \pm 0.002$
4)	$\text{CoMnSn}$	$P6_3/mmc$	$a=b=4.2809 \pm 0.0001, c=5.3638 \pm 0.0003$
5)	$\text{MnSn}$	$F-43m$	$a=b=c=6.1519 \pm 0.0002$
6)	$\text{SnO}$	$P4/nmm$	$a=b=3.79 \pm 0.03, c=4.85 \pm 0.01$

Table 3.2: List of phases that matched the Mn-Sn XRD data

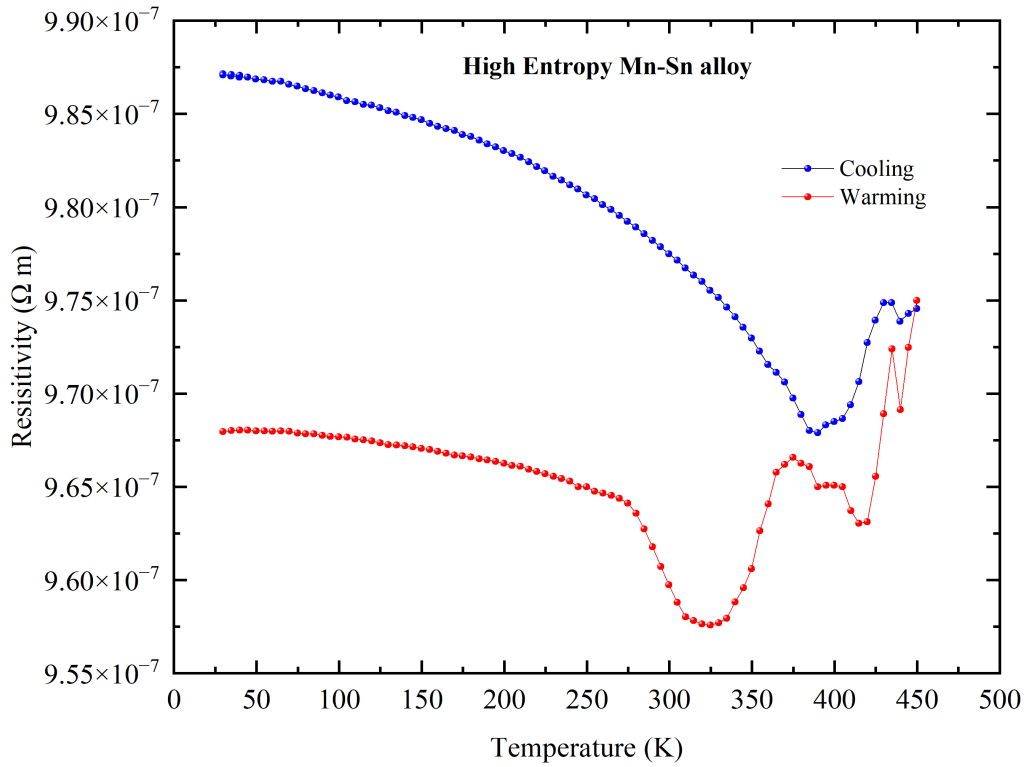


Figure 3.10: Resistivity plot for Mn-Sn alloy

Direct current resistivity measurements shown in Fig.3.10 indicate a decrease in resistivity with an increase in temperature but a sudden resistivity upturn is seen that suggests a structural and magnetic transition. On cooling, it was observed that resistivity increased showing a semiconductor(semi-metallic)like behavior. This is because in semiconductors the valence and conduction bands do not overlap. On increasing temperature, the electrons in the valence band gain sufficient thermal energies to jump to the conduction band. As the number of electrons in the conduction band increases, so conductivity increases and resistivity decreases [22].

## 3.4 High Entropy Fe-Sn alloy

### 3.4.1 Annealed at 1000 ° C



Figure 3.11: Sample fused together on annealing

On following the conventional high entropy preparation method it was observed that the pieces of the annealed sample melted and fused together as shown in Fig. 3.11.

Profile fitting of room temperature XRD pattern of high entropy Fe-Sn alloy shown in Fig. 3.12 suggested presence of multiple phases as listed below. The high intensity peaks matched the  $\text{Fe}_2\text{Sn}$  phase as compared to other phases.

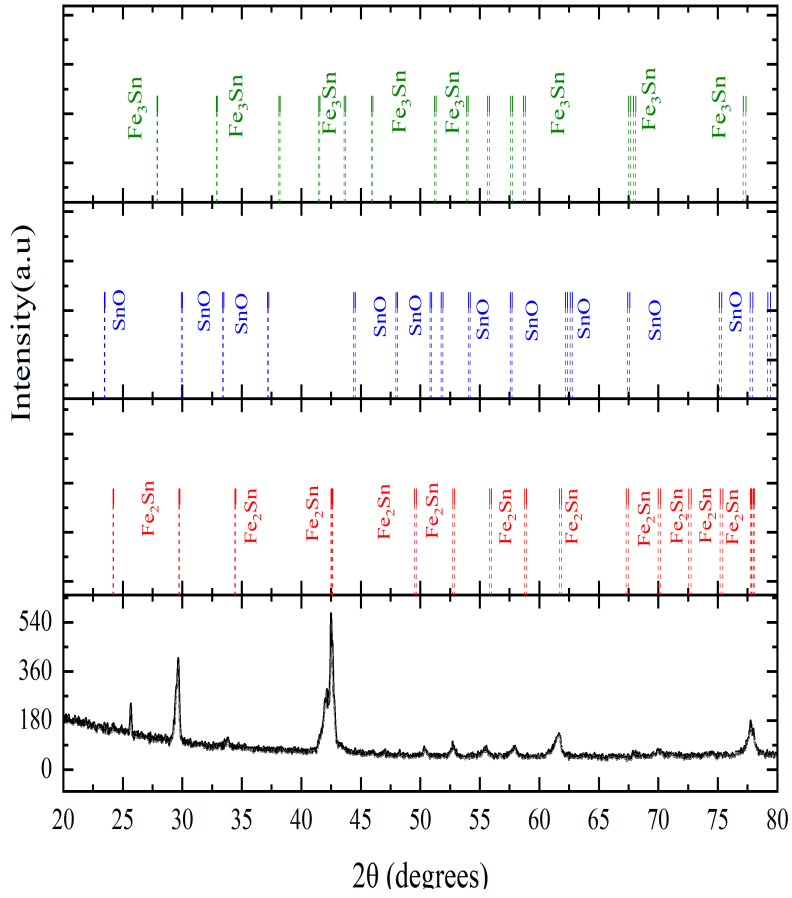


Figure 3.12: Phases that matched with XRD data of Fe-Sn alloy

Phases	Space group	Lattice constants( $\text{\AA}^\circ$ )
Fe <sub>3</sub> Sn	$P6_3/mmc$	$a=b=5.4471 \pm 0.0004$ , $c = 4.3512 \pm 0.0004$
SnO	$P4/nmm$	$a=b=3.7926 \pm 0.0005$ , $c=4.8294 \pm 0.0007$
Fe <sub>2</sub> Sn	$P6_3/mmc$	$a=b=4.2473 \pm 0.0003$ , $c=5.2075 \pm 0.0003$

Table 3.3: List of phases that matched the Fe-Sn XRD data

## 3.4.2 Annealed at 800°C

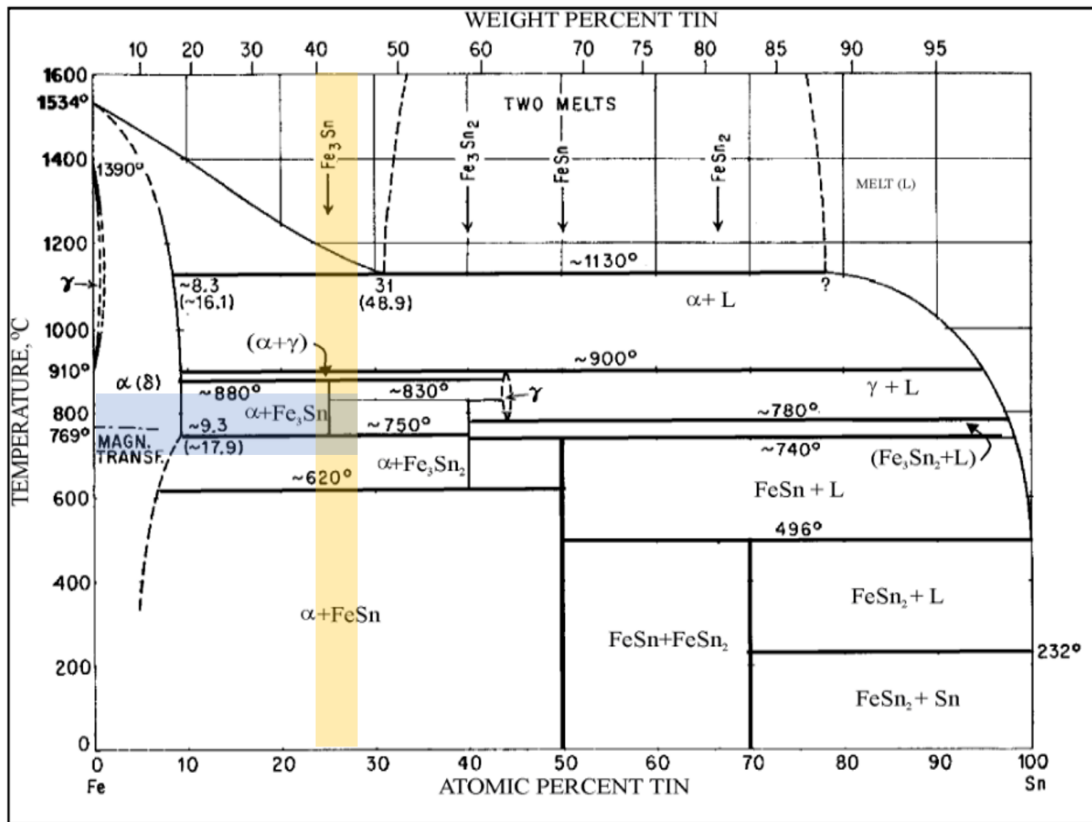


Figure 3.13: Fe-Sn phase diagram

The above Fe-Sn phase diagram [23] suggests formation of different phases on annealing at different temperatures and using certain concentration of Sn. The conventional  $Fe_3Sn$  annealing temperature and weight percentage was followed to synthesize the Fe-Sn alloy.

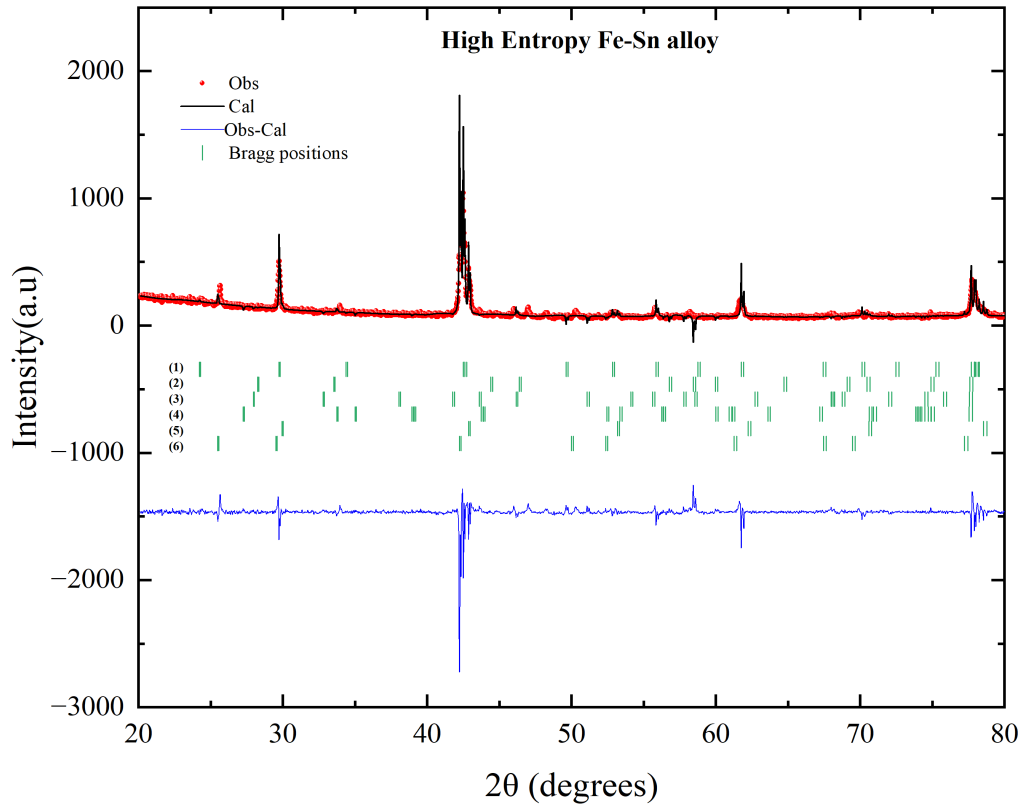


Figure 3.14: LeBail Fit of the XRD data for Fe-Sn alloy

No	Phases	Space group	Lattice constants( $\text{\AA}$ °)
1	$\text{Fe}_2\text{Sn}$	$P6_3/mmc$	$a=b= 4.24012 \pm 0.00007, c=5.2121 \pm 0.0002$
2	$\text{Fe}_3\text{Sn}_2$	$R-3m$	$a=b=5.339 \pm 0.001, c=20.8574 \pm 0.3569$
3	$\text{Fe}_3\text{Sn}$	$P6_3/mmc$	$a=b=5.458 \pm 0.001, c=4.3206 \pm 0.0009$
4	$\text{FeSn}_2$	$I4/mcm$	$a=b=6.535 \pm 0.003, c=5.310 \pm 0.002$
5	$\text{Fe}_{1.5}\text{Sn}_{0.5}$	$Pm-3m$	$a=b=c=2.9808 \pm 0.0002$
6	$\text{Fe}_2\text{SnTi}$	$Fm-3m$	$a=b=c=6.0472 \pm 0.0002$

Table 3.4: List of phases that matched the Fe-Sn XRD data

Profile fitting of room temperature XRD pattern of high entropy Fe-Sn alloy shown in Fig. 3.14 suggested presence of multiple phases as listed in 3.4. The high intensity peaks matched the  $\text{Fe}_2\text{Sn}$  phase as compared to other phases in this case too.

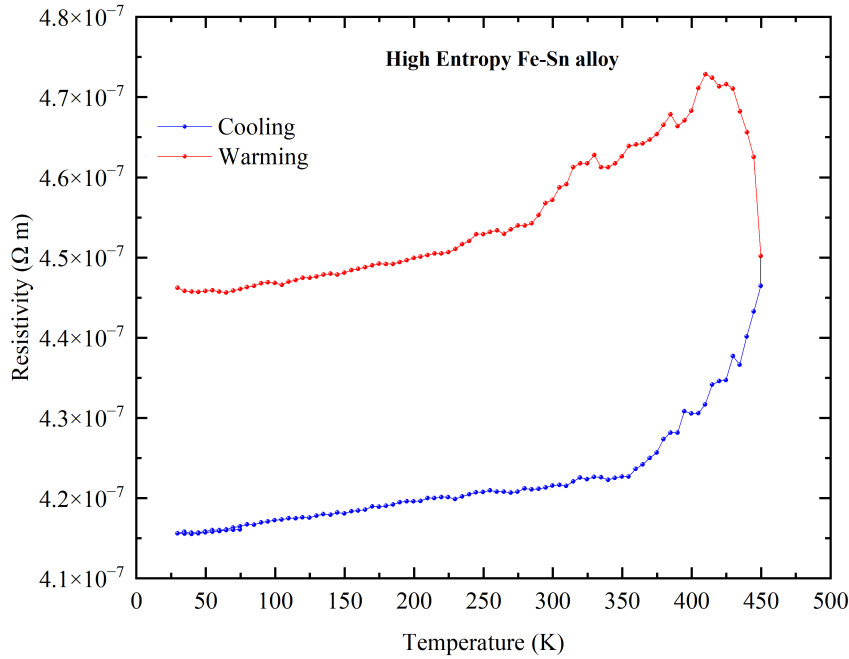


Figure 3.15: Resistivity plot for High entropy Fe-Sn alloy

The direct current resistivity measurements provide an effective tool to detect structural and magnetic transitions. As shown in Fig. 3.15 resistivity is observed to increase with increase in temperature and on cooling the resistivity decreases with temperature indicating a metallic like behaviour of the prepared Fe-Sn alloy [22]. This occurs because typically in metals the valence band and the conduction bands overlap. With increase in temperature the thermal motion among the atoms of the lattice increase. Charge carriers coincide into the lattice vibrations (phonons) more and this scattering increases the resistivity.

# Chapter 4

## Conclusion

In conclusion, systematic analyses of data obtained on following both the synthesis approaches show different behaviour from that shown by other high entropy alloys. On following the conventional high entropy synthesis method, melting all the elements together and quenching at 1000°C Sn leached out of the sample at high temperature. Normally high entropy alloys show a characteristic behaviour on following the same approach but our minor element being Sn melts at high temperature. Hence this method cannot be followed to obtain desired stabilized high entropy Mn-Sn, Fe-Sn synthesis. Secondly, for both the high entropy Fe-Sn sample data as shown in Fig 3.14 and 3.12 the highest intensity peaks match with  $\text{Fe}_2\text{Sn}$  phase. Thus we can understand that if taking stoichiometric weights of  $\text{Fe}_3\text{Sn}$  we can obtain a  $\text{Fe}_2\text{Sn}$  phase then on adding and balancing Fe and Sn weight percentage we can obtain a desired Fe-Sn alloy. Lastly, we can conclude that the weight percentage of each alloy used and annealing temperatures play an important role in high entropy alloy formation and are different from that compared to the pure stabilized Fe-Sn and Mn-Sn compounds.

# References

- [1] Db KC, Tilak Ram Thapaliya, Sebastian Parra, Xingyue Han, Jiajia Wen, Ryan Need, Pravin Khanal, Weigang Wang, Jiadong Zang, James Kikkawa, Liang Wu, and S Huang. Kondo physics in antiferromagnetic weyl semimetal  $\text{mn}_3\text{xsn}_1\text{x}$  films. *Science Advances*, 6, 08 2020.
- [2] Yang Zhang, Yan Sun, Hao Yang, Jakub Železný, Stuart P. Parkin, Claudia Felser, and Binghai Yan. Strong anisotropic anomalous hall effect and spin hall effect in the chiral antiferromagnetic compounds. *Physical Review B*, 95(7), Feb 2017.
- [3] Tomoya Higo, Danru Qu, Yufan Li, C. L. Chien, Yoshichika Otani, and Satoru Nakatsuji. Anomalous hall effect in thin films of the weyl antiferromagnet  $\text{mn}_3\text{sn}$ , Nov 2018.
- [4] *Advances in antiferromagnetic spintronics*, Jun 2022.
- [5] Hyun-Woo Bang, Woosuk Yoo, Kyujoon Lee, Young Haeng Lee, and Myung-Hwa Jung. Magnetic and structural phase transitions by annealing in tetragonal and cubic  $\text{mn}_3\text{ga}$  thin films. *Journal of Alloys and Compounds*, 869:159346, Jul 2021.
- [6] Banabir Pal, Binoy K. Hazra, Børge Göbel, Jae-Chun Jeon, Avanindra K. Pandeya, Anirban Chakraborty, Oliver Busch, Abhay K. Srivastava, Hakan Deniz, James M. Taylor, and et al. Setting of the magnetic structure of chi-

- ral kagome antiferromagnets by a seeded spin-orbit torque. *Science Advances*, 8(24), Jun 2022.
- [7] J. Yan, X. Luo, H. Y. Lv, Y. Sun, P. Tong, W. J. Lu, X. B. Zhu, W. H. Song, and Y. P. Sun. Room-temperature angular-dependent topological hall effect in chiral antiferromagnetic weyl semimetal  $\text{mn}_3\text{sn}$ . *Applied Physics Letters*, 115(10), Sep 2019.
- [8] Achintya Low, Susanta Ghosh, Susmita Changdar, Sayan Routh, Shubham Purwar, and S. Thirupathaiah. Tuning of topological properties in the strongly correlated antiferromagnet  $\text{mn}_3\text{sn}$  via fe doping, Oct 2022.
- [9] Xiaoyan Yang, Yi Qiu, Jie Su, Yalei Huang, Jincang Zhang, Xiao Liang, and Guixin Cao. Coexistence of in-plane and out-of-plane exchange bias in correlated kagome antiferromagnet  $\text{mn}_3\text{-xcrxsn}$ , Jul 2022.
- [10] Weidong Li, Peter K. Liaw, Weidong Li, and Peter K. Liaw. *High entropy materials: Challenges and prospects*. MDPI - Multidisciplinary Digital Publishing Institute, 2021.
- [11] Özge Özgün, David Koch, Asli Çak ır, Tolga Tavşanoğlu, Wolfgang Donner, Michael Farle, and Mehmet Acet. Magnetic properties of fcc and  $\sigma$  phases in equiatomic and off-equiatomic high-entropy cantor alloys. *Phys. Rev. B*, 106:214422, Dec 2022.
- [12] Chung-Chin Tung, Jien-Wei Yeh, Tao tsung Shun, Swe-Kai Chen, Yuan-Sheng Huang, and Hung-Cheng Chen. On the elemental effect of alcocrcrufeni high-entropy alloy system. *Materials Letters*, 61(1):1–5, 2007.
- [13] Che-Wei Tsai Chi Lee Chien-Chang Juan Ming-Hung Tsai, Kun-Yo Tsai and Jien-Wei Yeh. Criterion for sigma phase formation in cr- and v-containing high-entropy alloys. *Materials Research Letters*, 1(4):207–212, 2013.
- [14] Asl305; Ccedil;ak305;r, Mehmet Acet, and Michael Farle. A high-entropy b2 heusler alloy - high entropy alloys materials, Feb 2023.

- 
- [15] Yaşar Orbay, Ziyuan Rao, Aslı Çakır, Tolga Tavşanoğlu, Michael Farle, and Mehmet Acet. Magnetic properties of the fcc and bcc phases of (mnfeconi)<sub>80</sub>cu. *Acta Materialia*, 259:119240, Oct 2023.
- [16] J.L. Jorstad. Electric arc furnace melting. *Casting*, page 87–98, Dec 2008.
- [17] *World Pumps*, 2000(406):6, Jul 2000.
- [18] Pearl F Sequeira. *X-ray Diffraction: Principle and Application*. PhD thesis, 2022.
- [19] F. M. Smits and D. Schroder. Four point probe resistivity measurements.
- [20] G. J. DICKINS, AUDREY M. DOUGLAS, and W. H. TAYLOR. Structure of the sigma-phase in the iron–chromium and cobalt–chromium systems. *Nature*, 167(4240):192–192, Feb 1951.
- [21] H. Okamoto. Mn-sn (manganese-tin). *Journal of Phase Equilibria*, 20(5):542–542, Sep 1999.
- [22] Libretexts. Resistivity, Jul 2021.
- [23] *Research Journal of Life Sciences, Bioinformatics, Pharmaceutical and Chemical Sciences*, Aug 2017.